*Clays and Clay Minerals*, Vol. 60, No. 3, 315–329, 2012.

# MINERAL PREFERRED ORIENTATION AND MICROSTRUCTURE IN THE POSIDONIA SHALE IN RELATION TO DIFFERENT DEGREES OF THERMAL MATURITY

WARUNTORN KANITPANYACHAROEN[1], FRANS B. KETS[2], HANS-RUDOLF WENK[1,*], AND RICHARD WIRTH[3]

[1] Department of Earth and Planetary Science, University of California, Berkeley, CA, 94720 USA
[2] School of Earth and Environment, University of Leeds, Leeds LS2 9JT, UK
[3] GeoForschungsZentrum, Potsdam, 14473, Germany

**Abstract**—The thermal maturity of samples of the Posidonia Shale collected from the Hils Syncline, northern Germany, varies significantly as a function of location indicating variations in local history. Synchrotron X-ray diffraction was used to document the composition and the preferred orientation of four samples of the Posidonia Shale with different degrees of maturity (0.68−1.45%, $R_o$) to determine possible effects on diagenesis and preferred orientation. Overall, the degree of preferred orientation of all clay minerals (illite-smectite, illite-mica, and kaolinite) and in all samples is similar, with (001) pole figure maxima ranging from 3.7 to 6.3 multiples of a random distribution (m.r.d.). Calcite displays weak preferred orientation, with *c* axes perpendicular to the bedding plane (1.1−1.3 m.r.d.). Other constituent phases such as quartz, feldspars, and pyrite have a random orientation distribution. The difference in thermal history, which causes significant changes in the maturity of organic matter, influenced the preferred orientation of clay minerals only marginally as most of the alignment seems to have evolved early in their history. Synchrotron X-ray microtomography was used to characterize the three-dimensional microstructure of a high-maturity sample. Low-density features, including porosity, fractures, and kerogen, were observed to be elongated and aligned roughly parallel to the bedding plane. The volume of low-density features was estimated to be ~7 vol.%, consistent with previous petrophysical measurements of porosity of 8−10 vol.%. Transmission electron microscopy analysis of samples with different degrees of maturity (0.74%$R_o$ and 1.45%$R_o$) was used to document microstructures at the nanoscale as well as the presence of kerogen. In the high-maturity sample, pores were less abundant while minerals were more deformed as shown by fractured calcite and by kinked and folded illite. Some of the porosity was aligned with clay platelets.

**Key Words**—Clay Minerals, Microstructure, Porosity, Posidonia Shale, Preferred Orientation.

## INTRODUCTION

Shales are defined here as fine-grained sedimentary rocks containing a large proportion of clay minerals. Due to their sheet-like structure, these minerals align preferentially with (001) lattice planes parallel to the bedding plane during sedimentation, compaction, and diagenesis (Ho *et al.*, 1999). The compaction and recrystallization processes, in particular, lead to a reorientation of clay platelets, increased elastic and seismic anisotropy, an increase of clay mineral packing density, and a loss of porosity and permeability (*e.g.* Baker *et al.*, 1993; Hornby *et al.*, 1994; Sayers, 1994; Johansen *et al.*, 2004; Draege *et al.*, 2006; Bachrach, 2011). Recently, the potential for shales to act as unconventional reservoirs for natural gas has been recognized, which has increased interest in studying the physical and chemical characteristics of shale (*e.g.* Curtis *et al.*, 2010; Loucks *et al.*, 2009; Jenkins and Boyer, 2008; Martini *et al.*, 2003; Schulz *et al.*, 2010; Bernard *et al.*, 2010).

* E-mail address of corresponding author:
wenk@berkeley.edu
DOI: 10.1346/CCMN.2012.0600308

The mineralogical composition and microstructure of shales have been studied extensively, though the preferred orientation of clay minerals in these shales has been discussed less often. The preferred orientation of minerals and anisotropic pore space are important contributors to elastic and seismic anisotropy (Vernik and Nur, 1992; Hornby *et al.*, 1994; Kanitpanyacharoen *et al.*, 2011). Studies by Vernik (1993, 1994) suggested that the intrinsic anisotropy of organic-rich shales is further enhanced by bedding-parallel microfractures that were created during hydrocarbon generation. Due to the complex structure and poor crystallinity of clay minerals, quantification of preferred orientation is challenging. Several studies, which rely on traditional X-ray pole figure goniometry (*e.g.* Curtis *et al.*, 1980; Sintubin, 1994; Ho *et al.*, 1995, 1999; Aplin *et al.*, 2006; Valcke *et al.*, 2006; Day-Stirrat *et al.*, 2008a, 2008b) and on synchrotron X-ray diffraction (SXRD) techniques (*e.g.* Lonardelli *et al.*, 2007; Wenk *et al.*, 2008; Voltolini *et al.*, 2009; Wenk *et al.*, 2010; Kanitpanyacharoen *et al.*, 2011), have supplied evidence that the preferred orientation of clay minerals increases with increasing clay content, burial, and diagenesis. Given the diversity of shales and the dependence of preferred orientation on provenance, clay mineralogy, and bioturbation, the

variation of preferred orientation of minerals cannot be attributed to a single factor.

In the present study, shales of a single formation but with a variable thermal history were measured to investigate whether differences in thermal history have affected the preferred orientation patterns of constituent clay minerals. A SXRD technique was used to characterize the composition and preferred orientation of four Lower Jurassic Toarcian Posidonia Shale samples retrieved from the Hils Syncline in northern Germany (Figure 1). The samples varied in terms of vitrinite reflectance ($R_o$) from 0.68% in the SE to 1.45% in the NW (Littke and Rullkötter, 1987; Littke *et al.*, 1988). The variation indicates differences in local temperature history due to either a local igneous intrusion or a complex burial history (*e.g.* Leythaeuser *et al.*, 1980; Rullkötter *et al.*, 1988; Petmecky *et al.*, 1999). The three-dimensional (3D) distribution of porosity and constituent phases was investigated by synchrotron X-ray microtomography (SXM) and the results are compared with porosity measurements from other techniques (Mann *et al.*, 1986; Mann, 1987). Microstructures at the nanoscale were also studied by transmission electron microscopy (TEM).

## SAMPLES

The Lower Jurassic Toarcian Posidonia Shale is the main hydrocarbon source rock in the North Sea, offshore of The Netherlands, and in northern Germany (Rullkötter *et al.*, 1988; Littke *et al.* 1991, 1997; Doornenbal and Stevenson, 2010 and references therein). The Posidonia Shale is generally dark gray, laminated, and bituminous, and was deposited in a low-energy and oxygen-depleted environment. The shales represent peak transgression during a sea-level highstand and correspond to a global oceanic anoxic event dating back ~176 Ma (Doornenbal and Stevenson, 2010).

In the Hils Syncline of northern Germany (Figure 1) the properties of the Posidonia Shale vary considerably, depending on the burial depth, compaction, and local history (Littke and Rullkötter, 1987; Littke *et al.*, 1988). The low-energy environment rocks from the same sedimentary sequence are laterally continuous, with the main variability caused by organic content as a function of depth and stratigraphy (Littke *et al.*, 1991; Rullkötter *et al.*, 1988). Significant lateral variation in terms of the maturity of the organic content of Posidonia Shale retrieved at the Hils Syncline is due to the local history of the Lower Saxony Basin (Rullkötter *et al.*, 1988). Lateral differences in thermal maturity are believed to be caused by deep Cretaceous igneous intrusions (Deutloff *et al.*, 1980; Leythaeuser *et al.*, 1980; Rullkötter *et al.*, 1988), or, as was demonstrated for structures slightly west of the area of interest, by a combination of deep burial, substantial subsidence, and intense uplift processes of individual structures (Petmecky *et al.*, 1999; Muñoz *et al.*, 2007). The cause of the thermal anomalies is still under discussion (Kus *et al.*, 2005; Bilgili *et al.*, 2009).

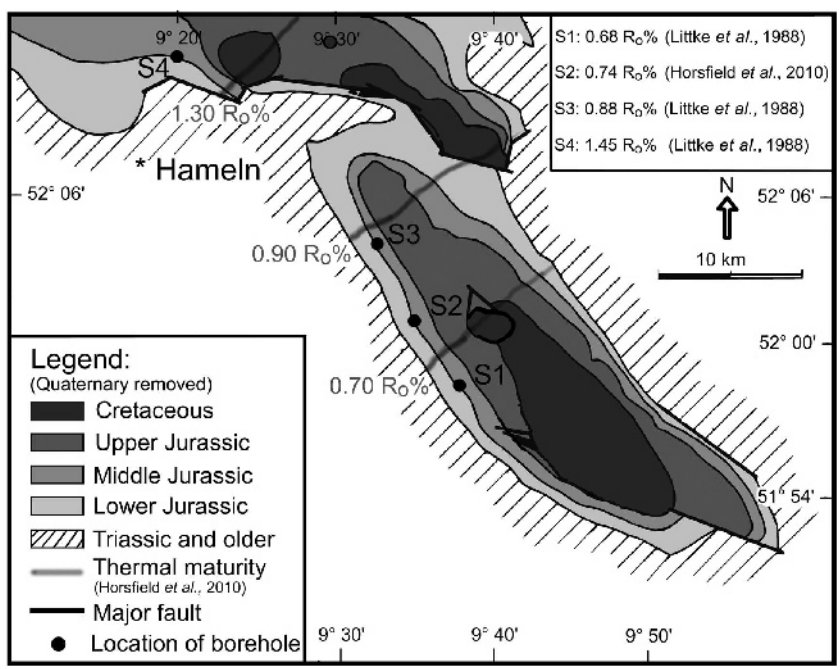


Figure 1. Geological map of the Posidonia Shale in the Hils syncline, indicating the samples (S1–S4) used in the present study (modifed from Littke *et al.*, 1988). Different thermal maturity ($R_o$%) contours (after Horsfield *et al.*, 2010) are also displayed.

https://doi.org/10.1346/CCMN.2012.0600308 Published online by Cambridge University Press

Four samples (S1–S4) of the Posidonia Shale retrieved from four different wells, ~10–20 km apart (Mann 1987, Figure 1), in the Hils syncline were studied. The samples were taken from the ~40 m thick Toarcian formation at a depth of ~50–60 m. No evidence has been found for significant variation in depositional environment over the sampled area (Littke *et al.*, 1988), but faulting has been diagnosed at the location of S4, leading to a locally greater porosity (Mann, 1987). The maturity of the organic matter, defined by vitrinite reflectance ($R_o$) (Tissot and Welte, 1984), ranged from 0.68 to 1.45% $R_o$ (Littke and Rullkötter, 1987; Littke *et al.* 1988; Bernard *et al.*, 2012; Horsfield *et al.*, 2010). As inferred from mercury injection (MICP), the porosity of the shales with similar degrees of thermal maturity obtained from the same set of wells was generally small, ranging from 4 to 10% (Mann, 1987), with porosity decreasing as a function of maturity.

## EXPERIMENTAL METHODS

### *Scanning electron microscopy*

A polished slice of sample S4 was coated with carbon and examined using a Zeiss Evo MA10 low-vacuum SEM, equipped with an EDAX Energy-dispersive Spectroscopy (EDS) system. The scanning electron microscope (SEM) was operated with an accelerating voltage of 30 kV and a probe current of 20 nA. The brightness variation of backscattered (BE)-SEM images (Figure 2a,b), ranging from low (black) to high (white), is due to the contrast in atomic number, with high atomic numbers giving white. The EDAX Genesis Imaging/Mapping software was used to collect compositional maps for Al, Si, O, Fe, Mg, and K (Figure 3), indicating an abundance of pyrite ($FeS_2$) and Fe- and Mg-containing illite.

### *Synchrotron X-ray diffraction*

Four shale samples were first embedded in low-temperature hardening epoxy resin in plastic containers to produce epoxy cylinders, ~2 cm in diameter. The shale-containing cylinders were then cut and polished into 2 mm slices. A monochromatic synchrotron X-ray beam, 1 mm in diameter and with a wavelength of 0.10779 Å, was used to collect diffraction patterns at the BESSRC 11-ID-C beamline of the Advanced Photon Source (APS) at Argonne National Laboratory (Chicago, Illinois, USA). Detailed information about the experiment setup has been given elsewhere (*e.g.* Wenk *et al.* 2008). The sample was mounted on a goniometer, translated parallel to the goniometer axis over different spots in 2 mm increments to obtain a representative sample volume. The sample slab was then tilted around the goniometer axis from –45º to 45º in 15º increments to obtain a significant pole-figure coverage. Diffraction patterns were recorded for 60 s with a Mar345 image plate detector (3450 × 3450 pixels), positioned at ~2 m from the sample. The angles ranged from 0 to 4.6º2θ in each diffraction pattern.

The instrument geometry (sample–detector distance, beam center, and image plate tilt) was first calibrated with a $CeO_2$ powder standard. The diffraction images with Debye rings were then 'unrolled' by integrating from 0 to a 360º azimuth over 10º intervals to produce 36 spectra, representing distinctively oriented lattice planes. A stack of these spectra for the 0º tilt image of S4 clearly indicated peak intensity variations with azimuth (Figure 4a, lower = experimental). The spectra are expressed as a function of $Q = 2\pi/d$ rather than $d$ (lattice spacing), where everything becomes compressed toward small lattice spacings. A $Q$ range of 0.37–3.70 $Å^{-1}$ ($d$ spacing 1.80–16.98 Å) was used. The diffraction spectra were then processed with the *MAUD* (*Material Analysis Using Diffraction*) software (Lutterotti *et al.*, 1997). The software relies on Rietveld refinement (Rietveld, 1969), which is a least-squares approach to minimize the difference between experimental diffraction data (Figure 4a, lower = experimental) and a calculated diffraction model (Figure 4a, upper

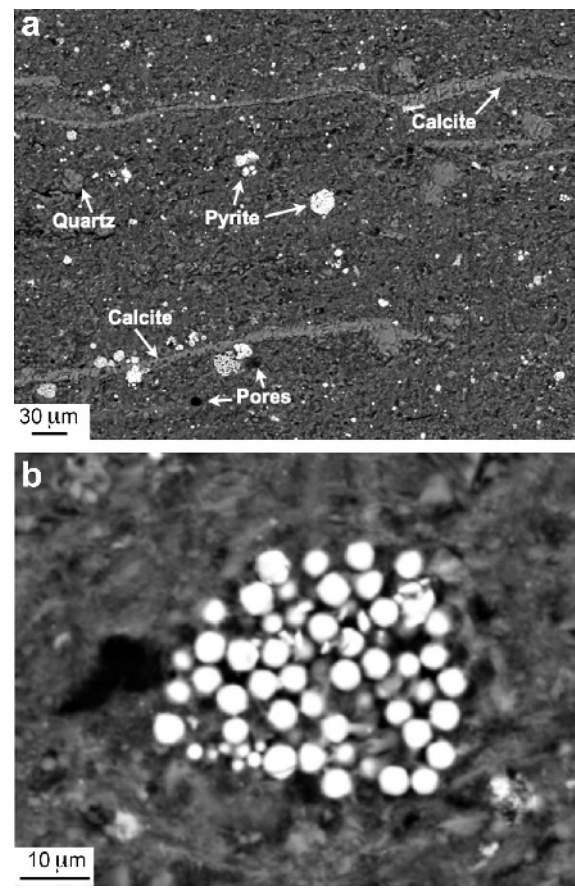


Figure 2. Backscattered SEM images of sample S4 illustrating (a) the microstructure of component minerals and (b) the presence of a pyrite framboid structure.

https://doi.org/10.1346/CCMN.2012.0600308 Published online by Cambridge University Press

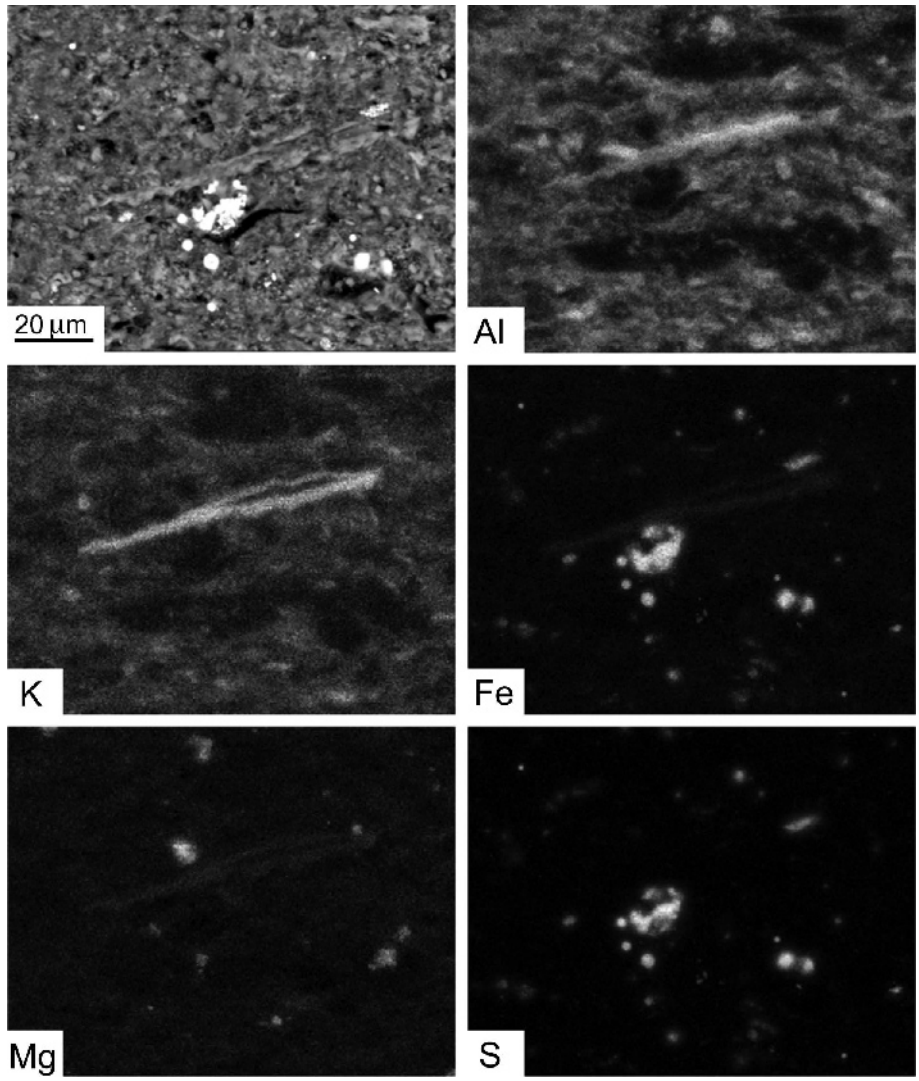


Figure 3. EDS analysis of sample S4 showing elemental maps of Al, K, Fe, Mg, and S, with an elongated illite-mica grain in the center.

= calculated). The calculated model is defined by several factors such as instrumental parameters, scattering background, crystal structure, microstructure, and volume fraction of each phase and its preferred orientation. Seven major minerals were recognized in the samples of the Posidonia Shale (Figure 4b, bottom).

The crystallographic structures of the clay minerals were obtained from the *American Mineralogist* Crystal Structure Database (Downs and Hall-Wallace, 2003; specifically, triclinic kaolinite from Bish, 1993; monoclinic illite-mica from Gualtieri, 2000; and monoclinic illite-smectite, based on a muscovite–phengite composition, from Plançon *et al*., 1985) whereas the structures for quartz, calcite, feldspar, pyrite, and dolomite were imported from the database contained in *MAUD*. For the Rietveld refinement of monoclinic phases, the first setting (with *c* as the unique axis) has to be used, but for representation the more conventional second setting (with *b* as the unique axis) is used with, in the case of monoclinic phyllosilicates, (001) as the cleavage plane. The spectra were refined with background polynomial functions, scale parameters, phase volume fraction, and lattice parameters, but atomic coordinates were kept constant. The peak shapes and widths were modeled by refining anisotropic crystallite size and microstrain. The preferred orientation was computed by the *EWIMV* algorithm (Matthies and Vinel, 1982), using 10º resolution for the orientation distribution determination, without imposing sample symmetry.

The orientation distribution, which defines the crystallite orientation relative to sample coordinates, was then exported from *MAUD* and imported into the *BEARTEX* software (Wenk *et al.*, 1998) to further process the orientation data. The orientation distribution

https://doi.org/10.1346/CCMN.2012.0600308 Published online by Cambridge University Press

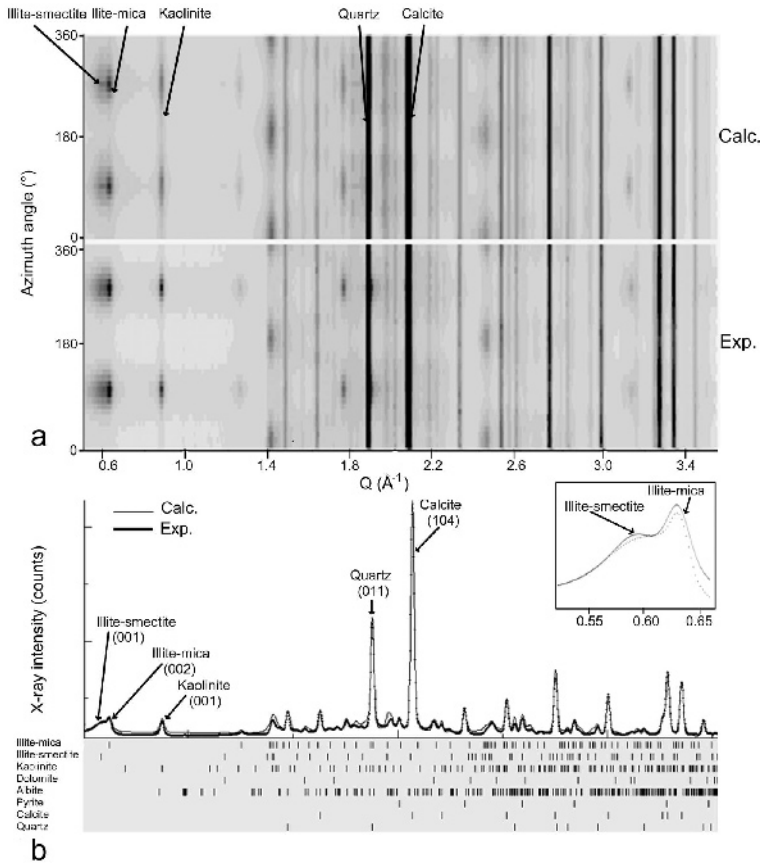


Figure 4. A comparison of (a) 'unrolled' diffraction spectra of sample S4 between the calculated model (upper) and the experimental data (lower) and (b) diffraction peaks in the spectrum which display eight constituent minerals. The variation in intensity along the azimuth are clearly displayed in (a) and are indicative of the preferred orientation for some minerals. The insert in (b) is an enlargement of the Q ~ 0.6 Å$^{-1}$ peak showing the overlapping 002 peaks of illite-mica and illite-smectite. The dotted line represents experimental data and the solid line is the Rietveld fit extracted.

was smoothed with a 7.5º filter to minimize artifacts from the orientation cell structures. The sample was rotated so that pole figures were defined with respect to the bedding plane. The pole densities are expressed as multiples of random distribution (m.r.d.). The basal plane (001) in clay minerals is most significant, thus the (001) pole figures are projected on the bedding plane, with the direction perpendicular to the bedding plane in the center of the pole figures (Figure 5).

*X-ray microtomography*

A small cylinder of sample S4, 1 mm in diameter and 5 mm long, was investigated using X-ray tomography at the TOMCAT (TOmographic Microscopy and Coherent rAdiology experimenTs) beamline of the Swiss Light Source (SLS) at the Paul Scherrer Institute in Villigen, Switzerland. The energy of the X-ray radiation was 16.0 keV, corresponding to a wavelength of 0.775 Å. A total of 1440 projections was recorded with a CCD detector (PCO2000), as the sample was rotated in 0.125º increments about the cylinder axis for 180º. More details about the beamline specifications have been described elsewhere (*e.g.* Stampanoni *et al.*, 2006; Marone *et al.*, 2009).

Each projection image represents a 2D X-ray absorption map. *Octopus* software (Dierick *et al.*, 2004) was used to normalize projections with background images and remove artifacts caused by the X-ray beam fluctuation and defects in the instruments, resulting in filtered images. The normalized data were then reconstructed into 3D images. A reconstructed slice was displayed parallel to the bedding plane or perpendicular to the cylinder axis (Figure 6a). The 3D array consisted of cubic cells (voxels) with grayscale values given as 16-bit integers. They are related to the rate of X-ray absorption per unit length (cm) of a given voxel. For calibration, the average grayscale on images outside the sample was subtracted from all values, resulting in grayscales ranging between −21.9 and 82.6. The lowest value (−21.9) corresponds to the darkest voxel while the largest value (82.6) indicates the brightest voxel. The zero grayscale value should not be construed as indicating zero absorption (Wang *et al.*, 2001). The voxel size was 0.74 μm × 0.74 μm × 0.74 μm.

https://doi.org/10.1346/CCMN.2012.0600308 Published online by Cambridge University Press

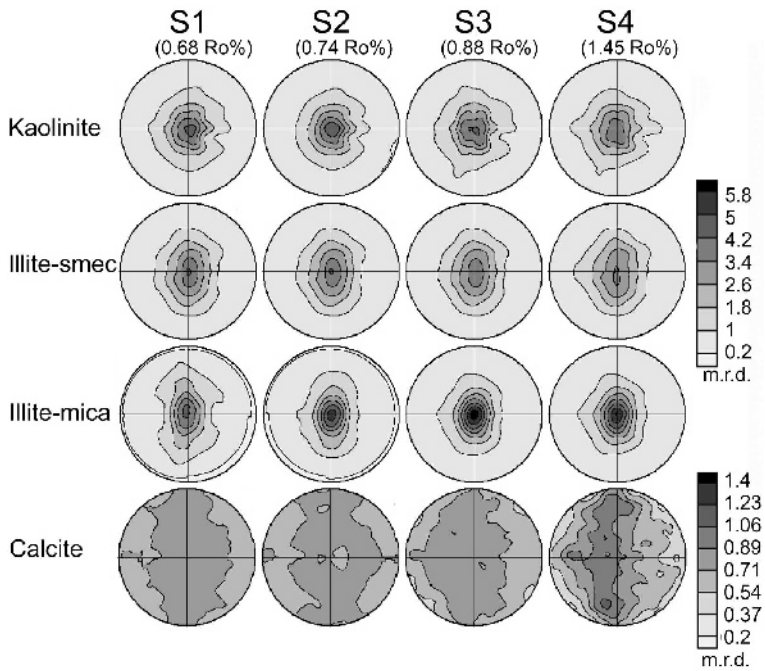


Figure 5. (001) pole figures for clay mineral phases and calcite in all samples. The pole densities are expressed in multiples of random distribution (m.r.d). Different scales are used for clay minerals and calcite. Equal area projection on the bedding plane.

A volume of $1000 \times 1000 \times 300$ voxels ($1.21 \times 10^8$ µm$^3$) inside the cylinder was selected for analysis using the *Avizo*® software (Visualization Sciences Group, www.vsg3d.com). A 3D median filter was first applied to avoid unnecessary blurring. The frequency distribution of grayscale values in logarithmic scale is shown in Figure 6b. A thresholding method on grayscale values was applied to differentiate between low-absorbing/low-density features (porosity, fractures, and organic matter or kerogen) and high-absorbing (pyrite) phases by visual inspection of microstructural features in the reconstructed images as shown in Figure 6a. Examples of areas in the reconstructed image (Figure 6a) correspond to grayscale values in Figure 6b. Area [1] indicates low-density features, including porosity, fractures, and kerogen; area [2] illustrates clay minerals, calcite, feldspars, and quartz; and area [3] displays pyrite grains. A threshold was set between the minimum grayscale (−21.9, darkest) and the maximum grayscale of the assumed low-density features (7.2). Segmentation for pyrite was carried out on a similar basis with the threshold range between the mininum (21.2) and the maximum grayscale values of pyrite (82.6, brightest). The intermediate gray shades were not segmented into different components (clay minerals, quartz, calcite, and feldspars) as they have very similar absorption characteristics. The 3D representation of low-density features, including porosity, fractures, and kerogen, as well as pyrite, is illustrated in Figure 7. The volume proportion, the size distribution, and the aspect ratio (length/width) of the components were also extracted from the chosen area (Figure 8).

*Transmission electron microscopy (TEM)*

Thin slices of samples S2 and S4, 10 µm × 5 µm × 0.15 µm in size, were prepared using a focused ion-beam thinning device (FEI FIB200TEM) and analyzed using an FEI Tecnai G2 X-Twin TEM at GeoForschungsZentrum (GFZ) at Potsdam, Germany. The instrument was equipped with a Gatan Tridiem energy filter, a Fishione high-angle annular dark-field (HAADF) detector, and an EDAX energy dispersive X-ray spectroscopy detector (EDS) for chemical characterization, as well as an electron energy loss spectrometer (EELS).

## RESULTS

Backscattered SEM images (Figure 2a,b) show complex microstructures of very fine-grained clay minerals, calcite veins, coarse-grained quartz, and pyrite. Pyrite is present as euhedral crystals and as fine-grained clusters of small octahedra in a framboid structure (<5 µm) (Figure 2b). Calcite-filled fractures are clearly aligned with the well developed horizontal bedding planes. Very fine-grained clay minerals are abundant in the matrix, in particular Fe- and Mg-containing detrital illite, which was verified by EDS elemental maps (Figure 3).

A summary of different phase proportions in weight fractions and lattice parameters, based on the Rietveld refinement, is given in Tables 1–2. In general, calcite (31–44 vol.%) and the illite-group (24–40 vol.%) dominate the composition in all samples. The amounts

https://doi.org/10.1346/CCMN.2012.0600308 Published online by Cambridge University Press

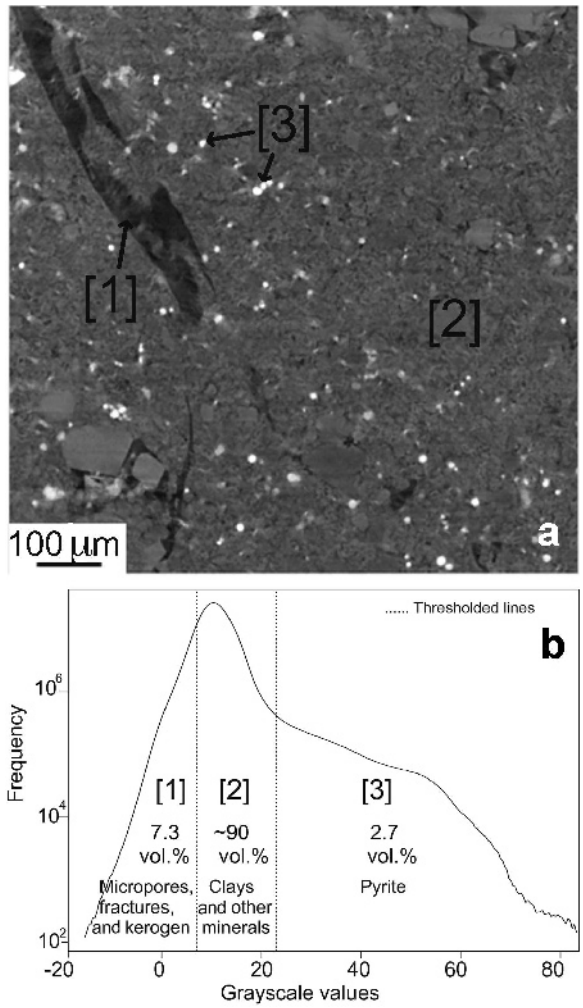


Figure 6. (a) A tomographic slice of an XY plane (bedding plane) and (b) histogram (in log scale) of grayscale values extracted from the selected area in the 3D reconstructed images of sample S4. Examples of different phases were identified: area [1] for micropores, fractures, and kerogen; area [2] for clay minerals, quartz, feldspars, and dolomite; and area [3] for pyrite.

of other phases such as quartz, kaolinite, pyrite, and albite are fairly similar. Dolomite was only observed in high-maturity samples S3 (0.88% $R_o$) and S4 (1.45% $R_o$). The weight proportions of different phases in this study are consistent with the proportions reported by Mann *et al.* (1986) and Mann (1987). The broad diffuse peak of illite-smectite (inset in Figure 4) indicates a low degree of crystallinity, small crystallite size, and stacking disorder.

The main focus of the present investigation was to quantify the preferred crystallographic orientation of the constituent minerals. The refined-model diffraction spectra (upper = calculated) were compared with experimental spectra (lower = experimental) in Figure 4a and they show a close similarity, indicative of an excellent fit, both in terms of intensity as well as the positions of the diffraction peaks. The average spectra for the 0º tilt images, with dots for experimental data and a thin solid line giving the calculated fit are shown in Figure 4b. Pole figures of preferred orientation analysis are displayed for kaolinite, illite-mica, illite-smectite, and calcite (Figure 5), with pole densities summarized in Table 3. Overall, the degrees of preferred orientation for the clay minerals are quite strong (3.7–6.3 m.r.d.) whereas orientation of quartz, albite, pyrite, and dolomite are close to random (pole figures are not shown). All pole figures are more or less axially symmetric with the (001) maximum perpendicular to the bedding plane, though no sample symmetry was imposed. Illite-mica, with a sharper (002) diffraction peak at lower *d* spacing, is generally coarse-grained and had a stronger preferred orientation (4.5 – 6.3 m.r.d.) than fine-grained illite-smectite (3.7–4.6 m.r.d.), with some variation between samples. Illite-mica in S3 has the strongest degree of preferred orientation with a (001) maximum perpendicular to the bedding plane of 6.3 m.r.d. Maximum pole densities of kaolinite and illite-smectite are similar in all samples (Figure 5). The

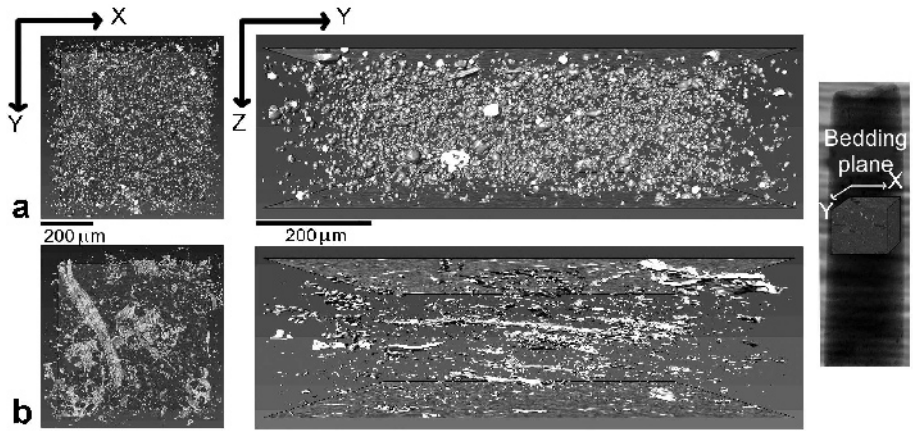


Figure 7. 3D Microtomography images of sample S4 showing the distribution of (a) pyrite and (b) micropores, fractures, and kerogen. X–Y is the bedding plance and direction Z is perpendicular to the bedding plane.

https://doi.org/10.1346/CCMN.2012.0600308 Published online by Cambridge University Press

Table 1. Quantitative phase proportions (wt.% upper row and vol.% lower row) of the mineral fractions, excluding porosity, extracted from the Rietveld refinement of the S1, S2, S3, and S4 samples.

| Sample | Kaolinite | Illite-smectite | Illite-mica | Calcite | Quartz | Albite | Pyrite | Dolomite |
|---|---|---|---|---|---|---|---|---|
| S1 | 7.95 | 11.76 | 11.24 | 43.82 | 16.21 | 2.30 | 6.71 | – |
| | 8.45 | 13.24 | 11.06 | 44.34 | 16.82 | 2.41 | 3.68 | |
| S2 | 10.56 | 12.50 | 17.48 | 37.25 | 16.66 | 0.99 | 5.59 | – |
| | 11.20 | 13.76 | 17.08 | 37.64 | 17.27 | 1.12 | 3.06 | |
| S3 | 5.91 | 22.06 | 14.79 | 33.18 | 16.58 | 2.49 | 4.49 | 1.50 |
| | 6.24 | 23.18 | 14.49 | 33.48 | 16.12 | 2.60 | 2.44 | 1.44 |
| S4 | 5.94 | 15.52 | 13.72 | 38.36 | 12.91 | 5.31 | 5.64 | 2.62 |
| | 6.37 | 16.94 | 13.46 | 38.72 | 13.36 | 5.54 | 3.08 | 2.51 |

(001) minima of clay mineral phases range from 0.1 to 0.5 m.r.d., suggesting a significant number of randomly oriented crystallites. Calcite grains also orient their *c* axes preferentially perpendicular to the bedding plane, but the alignment is much weaker than for clay minerals, ranging between 1.1 and 1.3 m.r.d.

The resolution of the microtomography image (Figure 6a) is comparable to that of the backscattered

Table 2. Lattice parameters obtained from the Rietveld refinement of the major phases. The parameters of albite and dolomite were kept constant throughout the refinement*. Monoclinic phases are displayed in the second setting system. Standard deviations of least significant digit in parentheses.

| Phase | Sample | *a* (Å) | *b* (Å) | *c* (Å) | α (º) | β (º) | γ (º) |
|---|---|---|---|---|---|---|---|
| Kaolinite | S1 | 5.18(1) | 8.98(1) | 7.44(1) | 92.13(2) | 105.06(2) | 89.31(1) |
| | S2 | 5.15(1) | 8.96(1) | 7.41(1) | 91.86(1) | 104.99(1) | 89.91(1) |
| | S3 | 5.17(1) | 8.98(1) | 7.43(1) | 92.14(1) | 104.06(2) | 89.29(1) |
| | S4 | 5.16(1) | 8.97(1) | 7.44(1) | 92.57(1) | 105.10(1) | 89.19(1) |
| Illite-smectite | S1 | 5.26(1) | 8.90(1) | 11.62(1) | 90.00 | 100.01(2) | 90.00 |
| | S2 | 5.29(2) | 8.94(2) | 11.46(1) | 90.00 | 99.87(2) | 90.00 |
| | S3 | 5.31(1) | 8.88(1) | 10.84(1) | 90.00 | 100.89(2) | 90.00 |
| | S4 | 5.45(1) | 8.91(1) | 10.89(1) | 90.00 | 100.29(1) | 90.00 |
| Illite-mica | S1 | 5.25(1) | 9.06(1) | 20.34(1) | 90.00 | 95.09(1) | 90.00 |
| | S2 | 5.20(2) | 9.00(3) | 20.12(2) | 90.00 | 95.87(1) | 90.00 |
| | S3 | 5.25(1) | 9.06(1) | 20.34(1) | 90.00 | 95.37(1) | 90.00 |
| | S4 | 5.28(2) | 9.03(2) | 20.44(2) | 90.00 | 95.24(1) | 90.00 |
| Calcite | S1 | 4.99(1) | 4.99(1) | 17.06(1) | 90.00 | 90.00 | 120.00 |
| | S2 | 4.99(1) | 4.99(1) | 17.06(1) | | | |
| | S3 | 4.99(1) | 4.99(1) | 17.05(1) | | | |
| | S4 | 4.99(1) | 4.99(1) | 17.06(1) | | | |
| Quartz | S1 | 4.91(1) | 4.91(1) | 5.41(1) | 90.00 | 90.00 | 120.00 |
| | S2 | 4.92(1) | 4.92(1) | 5.40(1) | | | |
| | S3 | 4.92(1) | 4.92(1) | 5.40(1) | | | |
| | S4 | 4.92(1) | 4.92(1) | 5.40(1) | | | |
| Albite* | S1 | 8.14 | 12.79 | 7.16 | 94.33 | 116.57 | 87.65 |
| | S2 | | | | | | |
| | S3 | | | | | | |
| | S4 | | | | | | |
| Pyrite | S1 | 5.42(1) | 5.42(1) | 5.42(1) | 90.00 | 90.00 | 90.00 |
| | S2 | 5.42(1) | 5.42(1) | 5.42(1) | | | |
| | S3 | 5.41(1) | 5.41(1) | 5.41(1) | | | |
| | S4 | 5.41(1) | 5.41(1) | 5.41(1) | | | |
| Dolomite* | S1 | – | – | – | – | – | – |
| | S2 | – | – | – | – | – | – |
| | S3 | 4.81 | 4.81 | 16.08 | 90.00 | 90.00 | 120.00 |
| | S4 | 4.81 | 4.81 | 16.08 | 90.00 | 90.00 | 120.00 |

https://doi.org/10.1346/CCMN.2012.0600308 Published online by Cambridge University Press

Table 3. Pole densities for (001) pole figures of kaolinite, illite-smectite, illite-mica, and calcite (m.r.d.).

| Sample | — Kaolinite — | | – Illite-smectite – | | — Illite-mica — | | — Calcite — | |
|---|---|---|---|---|---|---|---|---|
| | Min | Max | Min | Max | Min | Max | Min | Max |
| S1 | 0.29 | 4.38 | 0.48 | 4.58 | 0.16 | 4.51 | 0.92 | 1.07 |
| S2 | 0.11 | 4.83 | 0.44 | 4.44 | 0.18 | 5.35 | 0.81 | 1.09 |
| S3 | 0.29 | 4.24 | 0.47 | 4.27 | 0.26 | 6.30 | 0.89 | 1.11 |
| S4 | 0.28 | 3.86 | 0.47 | 3.67 | 0.27 | 5.31 | 0.78 | 1.25 |

SEM image (Figure 2a), *i.e.* slightly better than 1 μm. The high-absorbing materials are mainly pyrite and the distribution of these particles is scattered and does not appear linked to the bedding-plane orientation (Figure 7a). Based on segmentation using *Avizo*, the proportion of pyrite in S4 was estimated at 2.7 vol.%, which is consistent with the amount obtained from Rietveld analysis (3.1 vol.%) as well as the fraction reported by Mann (1987) (3–4 wt.% or ~2 vol.%). Intermediate gray shades, representing calcite, quartz, and clay minerals, are approximated at 90 vol.%. The volume fraction of low-density features, taken to be indicative of porosity, fractures, and kerogen (Figure 7b), was estimated at 7.3 vol.%. The low-absorbing features range in size from 500 $\mu m^3$ to 1 $\mu m^3$, which is considered to be the limit of the resolution. Small pore volumes (1–10 $\mu m^3$) clearly dominate (Figure 8a), though their contribution to the total volume may not be as significant. Pores are anisotropic, mostly disc shaped with high aspect ratios (Figure 8b), and organized mainly parallel to the bedding plane, with little connectivity in the flat porous zones in the direction perpendicular to the bedding plane (Figure 7b). A few horizontal fractures, which are probably a result of pore growth and coalescence or of unloading as a result of uplift, were also observed. Due to the limitation of resolution in microtomography, only pores and fractures in micron-scale and larger can be investigated adequately by this method. The volume percentage of low-density features determined with microtomography does not, therefore, represent the total porosity, fracture, and kerogen content.

The TEM images provide important additional information and insights into the material distribution at the μm to nm scale. The TEM investigations were performed on small regions of focused ion beam (FIB) slices, which may not be representative of the whole sample. The TEM images of the low-maturity sample S2 (0.74% $R_o$) illustrate an open framework of calcite fragments and some quartz (Figure 9a). The grain size was ~1 μm in diameter. Clay mineral platelets, mainly illite-smectite with some Mg, occur as clusters in interstitial pockets and along grain boundaries. The orientation of platelets is variable, but the overall direction is parallel to the bedding plane (vertical direction in Figure 9a). Open pores (black, Po) and kerogen (gray, Ke) are visible in the TEM image (Figure 9a). Organic matter does not cause diffraction effects such as Bragg fringes, and thus it appears uniformly gray in Figure 9a. Porosity is visible as white areas in a TEM bright-field image (Figure 9b). A number of pores are elongated following the clay platelet structure and, hence, organized roughly subparallel to the bedding plane (horizontal) while some are more equiaxial or spherical, ranging between 2 and 20 nm in diameter. They can be referred to as mesopores according to the IUPAC (1997) nomenclature. The TEM dark-field image (Figure 9a) and TEM bright-field image (Figure 10a) indicate that quartz is partially dissolved near the rim. Quartz and calcite show weak deformation with some dislocations and subgrains. The elemental composition of organic matter was verified by EELS scans of carbon and sulfur. The gray areas of elemental maps (Figure 10b–c) indicate carbon and

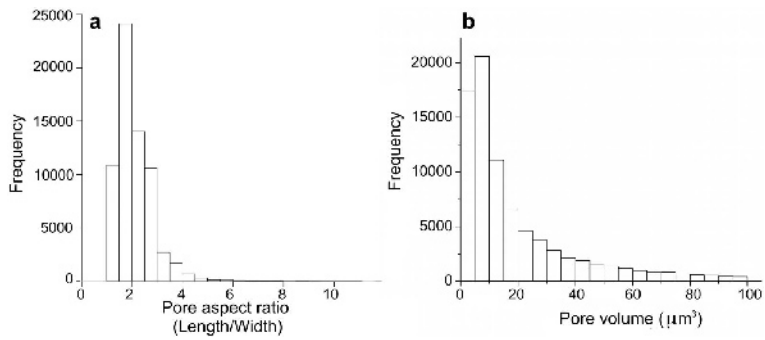


Figure 8. Histogram plots showing the frequency of (a) pore aspect ratio and (b) pore volume in the selected area shown in Figure 7b. The pore distribution and geometry were extracted from the segmentation data shown in Figure 7b.

https://doi.org/10.1346/CCMN.2012.0600308 Published online by Cambridge University Press

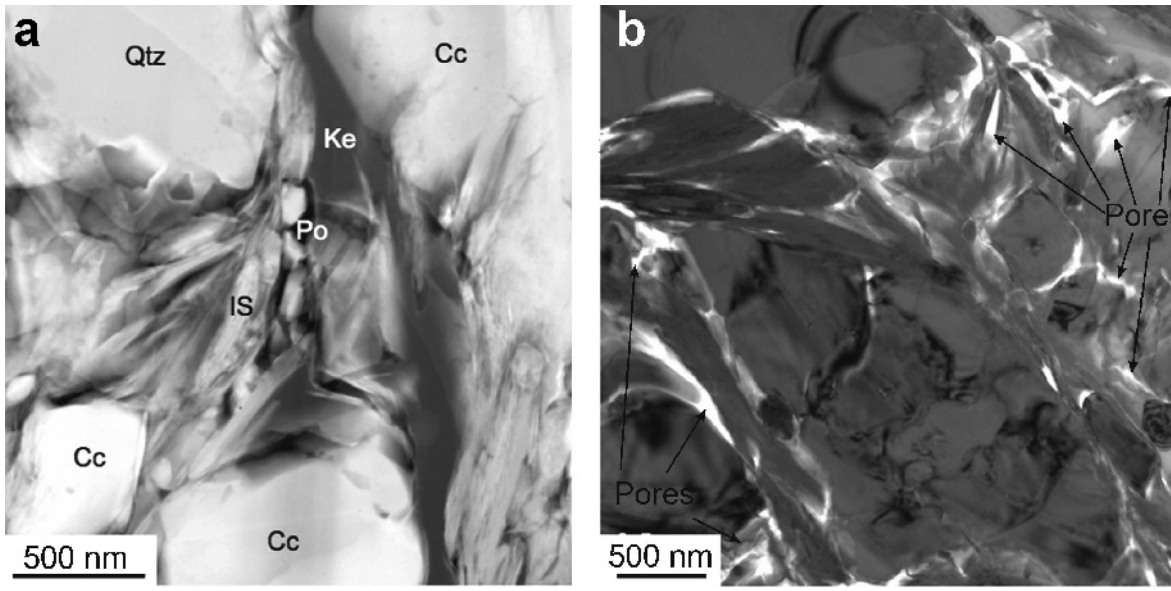


Figure 9. Microstructures in the low-maturity sample S1. (a) HAADF (high-angle annular dark-field) image illustrates the microstructure with black pores (Po), gray kerogen (Ke), grains of calcite (Cc) and quartz (Qtz), and clusters of illite-smectite (IS); (b) TEM bright-field image illustrating high porosity (light) between phyllosilicate platelets, a large calcite grain with dislocations and its subgrains (center), and a quartz grain (top) with pores.

some sulfur, which is absent from the surrounding calcite, illite-smectite, and quartz.

The TEM dark-field images of high-maturity sample S4 (1.45% $R_o$) (Figure 11a) show finer grain size and less porosity than those of sample S1. A TEM bright-field image (Figure 11b) illustrates high concentrations of dislocations in calcite, with subgrain formation and mechanical twins. Illite-smectite stacks are kinked and bent. Several sets of 11 Å fringes and bending of lattice planes are displayed in high-resolution images (inset in Figure 11c). Illite-smectite (with some Mg) is interlayered with a carbon-rich phase, presumably kerogen (Figure 11a). Some small crystallites of kaolinite (established by EDS, not shown) were also observed,

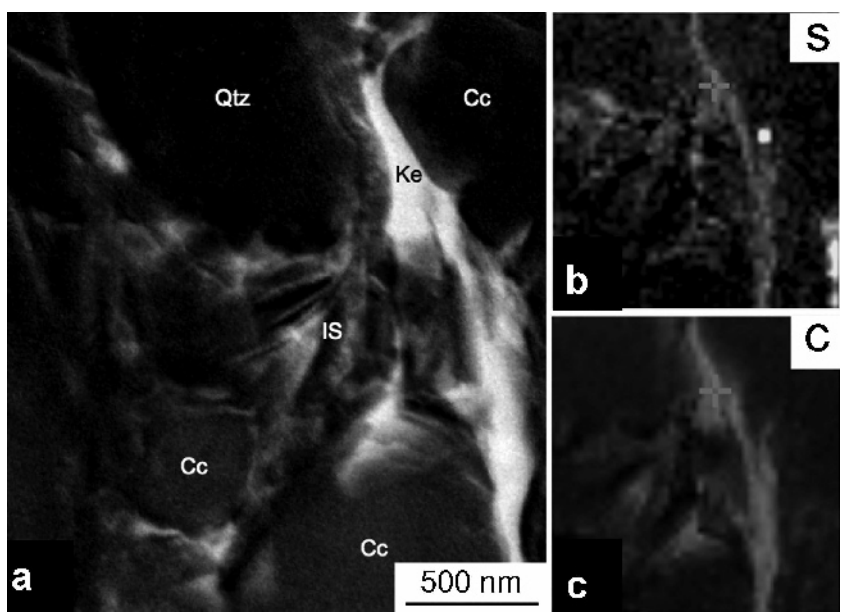


Figure 10. TEM bright-field image (a) and EELS (electron energy loss spectroscopy) maps of carbon C-K edge (b), and sulfur L-edge (c) of sample S1, both corrected for extrapolated background. The light regions correspond to kerogen with correlation of high C and S.

https://doi.org/10.1346/CCMN.2012.0600308 Published online by Cambridge University Press

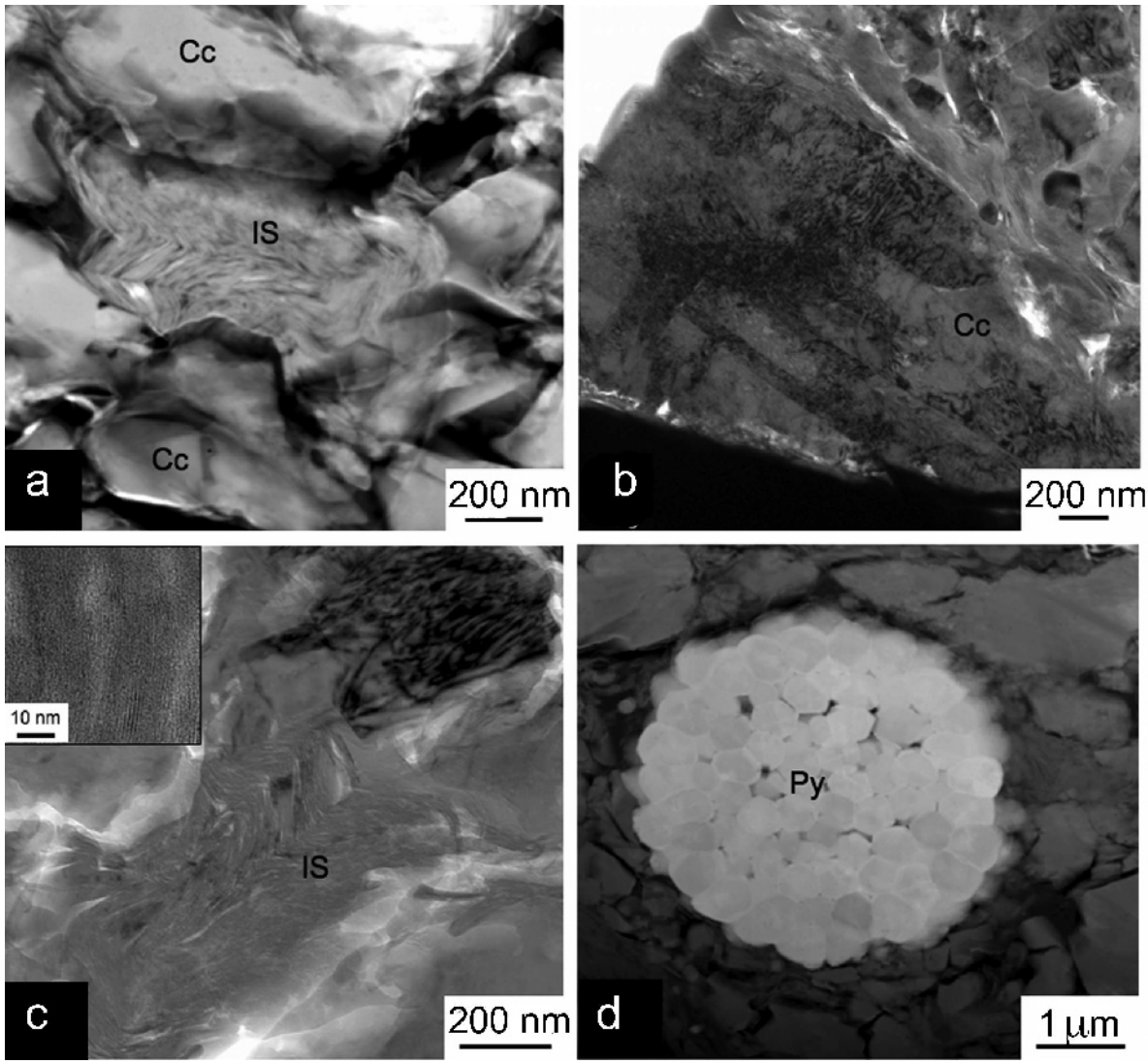


Figure 11. Microstructures in high-maturity sample S4. (a) HAADF image illustrating kinked illite-smectite and fractured calcite fragments; (b) TEM bright-field image of calcite with dislocations, subgrains, and mechanical twins and fluid inclusions; (c) TEM bright-field image showing kinks in illite-smectite and deformed calcite with the inset showing a high-resolution image of illite-smectite with 11 Å (001) stacking showing bending of lattice planes; and (d) HAADF image of the framboidal structure of pyrite.

with moderate preferred orientation. Framboid aggregations of pyrite are commonly found (Figure 11d), corresponding to those imaged by SEM (Figure 2b) and microtomography (Figure 7a).

## DISCUSSION

Care must be taken not to over interpret the differences observed between the four samples in the present study, though they were acquired at similar depths in the same stratigraphic unit, but possibly in slightly different stratigraphic positions. Small samples on the mm and μm scale were analyzed and thus the sophisticated analytical methods precluded statistical tests about variability.

### *Mineralogy*

Previous mineralogical studies of the Posidonia Shale based on bulk- and fine-fraction XRD (Mann, 1987; Littke *et al.*, 1988) showed no systematic dependence of the mineralogy on the maturity and exposure to different temperatures. Similarly, based on Rietveld analysis of SXRD images, all samples have similar mineralogical composition, with the illite group (24–40 vol.%) and calcite (31–44 wt.%) dominant. No clear evidence for diagenetic transformations of clay minerals was observed. Dolomite in high-maturity samples may be indicative of elevated temperatures; small amounts of albite are also present in the high-maturity samples, but the relevance of this is not clear.

https://doi.org/10.1346/CCMN.2012.0600308 Published online by Cambridge University Press

*Preferred orientation*

Previous work by Mann (1987) suggested a gradual decrease in porosity with maturity, with an exception noted for the Haddessen well, located in a more faulted area (corresponding to sample S4). The reduction in porosity with maturity has been interpreted as being due to increased cementation and/or increased depth of burial. Similarly, a trend can be observed as an increase in preferred orientation with maturity in illite-mica for low-maturity samples (S1: 0.68% $R_o$, S2: 0.74% $R_o$, and S3: 0.88% $R_o$), with a slight reversal trend for a high-maturity sample (S4: 1.45% $R_o$) (Table 3). Illite-mica in S3 has the strongest alignment with a (001) maximum of 6.3 m.r.d. A slight variation in the degree of preferred orientation between illite-smectite and kaolinite was observed in all samples. No trends which were functions of maturity could be ascertained from the degree of preferred orientation of illite-smectite and kaolinite, except that S4 had the least preferred orientation for both of these minerals. A considerable proportion of clay crystallites in all samples was oriented randomly, expressed by (001) minima of 0.1−0.3 m.r.d. for kaolinite, 0.2−0.3 m.r.d. for illite-mica, and 0.4−0.5 m.r.d. for illite-smectite. The orientation distributions of quartz, albite, dolomite, and pyrite were nearly random, close to 1 m.r.d. Interestingly, calcite has a weak but significant preferred orientation, ranging from 1.1 to 1.3 m.r.d. in (0001) pole figures (Figure 5). The maximum preferred orientation of calcite was observed in sample S4.

The trends observed in preferred orientations of clay minerals, notably the increasing trend of illite-mica, may not be statistically significant, as variability between samples, even taken centimeters apart, can be considerable. The thermal maturity did not seem to be a major effect on the degree of preferred orientation of clay minerals, suggesting that the clay mineral alignment formed early either at the period of consolidation (Baker *et al.*, 1993) or during diagenesis (Day-Stirrat *et al.*, 2008b).

*Microstructure*

Continuous layers of calcite, such as the veins illustrated in Figure 2a, may be related to cementation. The SEM image of sample S4 shows that calcite mostly aligns as horizontal veins parallel to the bedding plane. Higher maturity samples (S3 and S4) were exposed to greater temperatures, which may have reduced the organic content and increased the already large carbonate content (Rullkötter *et al.*, 1988). Carbonates in S3 and S4 had been altered diagenetically to dolomite, possibly due to decomposition of organic matter (Slaughter and Hill, 1991).

Unlike some other shales, *e.g.* from the Qusaiba Formation (clay minerals ~ 66 vol.%) (Kanitpanyacharoen *et al.*, 2011), Mt. Terri (clay minerals ~ 70 vol.%) (Wenk *et al.*, 2008), and the North Sea (clay minerals ~ 78%) (Wenk *et al.*, 2010), clay minerals do not dominate the microstructure of the Posidonia Shale (35−47 vol.%). The TEM images (Figure 9−11) show clearly that calcite is abundant with fragments more closely packed in S4 than in S2. Different generations of calcite were observed: (1) older fragmented calcite appears to be purer than (2) second-generation crystallites which are less deformed, and (3) those that occur in euhedral clusters and are enriched in Sr. The weak calcite alignment in S4 can be attributed to a shape alignment of calcite fragments which are preferably broken along cleavage planes $r = \{10\bar{1}4\}$, and to growth of crystals in younger and less deformed veins, which resulted from cementation of fractures. Organic matter is often interlayered with clay minerals (Figure 9a, 10a). Clay minerals occur as pockets in interstitial space and along calcite grain boundaries. In general, clay platelets tend to align parallel to the bedding plane, but with considerable dispersion. In some clusters, kaolinite occurs as fine crystallites in pores (Figure 10b), which is quite different from the kaolinite crystallites in Kimmeridge Shale that are very strongly oriented (Militzer *et al.*, 2011). The high maturity sample (S4: 1.45% $R_o$), retrieved from a more tectonically disturbed area, is clearly deformed as illustrated by kinked and folded clay minerals, fractured calcite fragments with mechanical twins, and large dislocation densities. The observations imply considerable local stresses, probably associated with compaction of tectonic origin (burial, uplift). The strong deformation in S4 may have contributed to a relatively weak preferred orientation. The observation of stress-related phenomena in S4, and the presence of late carbonate veins as well as the marginal increase of preferred orientation of illite-mica in S1−S3 as a function of thermal maturity, are consistent with a scenario in which the Posidonia Shale was buried and uplifted (Petmecky *et al.*, 1999; Muñoz *et al.*, 2007).

*Porosity analysis*

Total pore volume, including organic matter and pore-structure anisotropy, are relevant for the determination of elastic properties in shales. Low-density features, including porosity, fractures, and kerogen, were investigated by X-ray microtomography (XRM) and correspond to ~7.3 vol.%. The 3D representation (Figure 7b) as well as the distribution of volume and aspect ratio of these features (Figure 8) show that they are mostly dispersed, small (<10 $\mu m^3$), and flat (aspect ratio 1.5−2.5). Fractures and kerogen are usually aligned parallel to the bedding plane, larger (>10 $\mu m^3$), and more elongated (aspect ratio >2.5). Horizontal fractures may be created for several reasons such as pore growth and coalescence, unloading as a result of uplift (Petmecky *et al.*, 1999; Muñoz *et al.*, 2007), and sampling or drying of the cores. The aspect ratio of pores and fractures can play a significant role in the elastic anisotropy of shale.

https://doi.org/10.1346/CCMN.2012.0600308 Published online by Cambridge University Press

Based on the segmentation of the 3D voxel array, one can calculate the volume fraction of low-density features, including pores, fractures, and kerogen, but cannot quantify the total volume of porosity, which includes pores at nanoscale. Macro- (>50 nm), meso- (2−50 nm), and micropores (<2 nm) (according to IUPAC (1997) nomenclature) are substantially smaller than the pixel size (~0.7 μm), which is the limit of the microtomography technique used here. Pores at various nanoscales were observed in SEM and TEM images (Figures 2, 9−11). Judging from TEM images, the volume fraction of macro-, meso-, and micropores is ~2−5 vol.% (*e.g.* Figures 9b, 11b). While some pores in sample S2 are spherical (*e.g.* at triple junctions of calcite fragments), most are plate-shaped and are approximately parallel to the bedding plane (Figure 10a−b). The platy pores frequently bound with larger clay crystals. The flat pores imaged by TEM (Figure 9−11) are mostly found parallel to the bedding plane, possibly due to pore growth and coalescence, or to the unloading of the sample when uplifted to the current shallow depth. The same unloading mechanism may have caused fractures later filled with calcite observed in SEM and XRM.

Mann (1987) reported pore-throat sizes of between <2.2 nm and 60 nm, which are comparable with those of sealing shales as documented by Best and Katsube (1995) with mercury injection measurements. The pore sizes reported by Curtis *et al*. (2010) for gas shales were between ~5 nm and ~150 nm on the basis of FIB-SEM, nuclear magnetic resonance, and mercury-injection porosimetry measurements. Intraparticle organic pores (<75 μm) and pyrite-framboid intercrystalline pores were also identified by Ar-ion-milling in the SEM (Loucks *et al.*, 2009). Macro-, meso-, and micropores are beyond the resolution of the XRM measurements. For nanoscale resolution, 3D mapping methods have been developed for TEM (Midgley *et al*. 2007), FIB etching (Elfallagh and Inkson, 2009; Keller *et al.*, 2011), synchrotron X-ray nanotomography (Heim *et al.* 2009), and scanning transmission X-ray microscopy (Holzner *et al.* 2010; Bernard *et al.* 2010). Further study of the porosity and appropriate statistical averaging methods are necessary to understand in detail the macroscopic physical properties, especially elastic anisotropy, of Posidonia Shale.

## CONCLUSIONS

The present study focused on a quantification of the preferred orientation of clay minerals in samples of the Posidonia Shale from the Hils syncline in northern Germany, subjected to variable local histories. The preferred orientation of kaolinite, illite-mica, illite-smectite, and calcite was measured with SXRD techniques and quantified by Rietveld refinement. The degree of preferred orientation of clay minerals and calcite in all four samples with different maturity histories is comparable. Kaolinite and illite-mica generally exhibit stronger preferred orientations than microcrystalline illite-smectite. The difference in local history, which caused significant changes in the maturity of organic matter, did not influence the preferred orientation to a large extent and, thus, most of the preferred mineral orientation evolved rather early. The pore structure was investigated by SXM and TEM, suggesting that pores are mostly small (<10 $\mu m^3$), platy (aspect ratio >1.5), and layered in the bedding plane but not well connected. The low porosity of the high-maturity sample was due to carbonate cementation and deformation, consistent with previous measurements.

## ACKNOWLEDGMENTS

This project was supported by NSF (EAR-0836402) and DOE (DE-FG02-05ER15637). The authors thank Dr Volker Dieckmann (Shell International Exploration and Production) for providing samples used in the present research and Dr Johannes Wendebourg (Shell) for his permission to use these samples in this work. The material was acquired by Dr Ulrich Mann (FZ Jülich) and used in earlier studies. The authors acknowledge access to beamline 11-ID-C at the APS, the assistance of Yang Ren with diffraction experiments, access to the TOMCAT beamline at SLS, and assistance from Rajmund Mokso with the tomography experiments. The authors appreciate the help from Timothy Teague with sample preparation, Luca Lutterotti for updating the *MAUD* software to analyze these complex shale samples, Dula Parkinson for advice on analysis of tomographic data, access to the *Octopus* and the *Avizo* software at beamline 8.3.2 at ALS, and Anja Schreiber for kindly preparing the TEM samples. The authors thank Andrew Aplin and Manuel Sintubin for useful comments which helped to improve the manuscript.

## REFERENCES

Aplin, A.C., Matenaar, I.F., McCarty, D.K., and van der Pluijm, B.A. (2006) Influence of mechanical compaction and clay mineral diagenesis on the microfabric and pore-scale properties of deep-water Gulf of Mexico mudstones. *Clays and Clay Minerals*, **54**, 500−514.

Bachrach, R. (2011) Elastic and resistivity anisotropy of shale during compaction and diagenesis: Joint effective medium modeling and field observations. *Geophysics*, **76**, E175−E186.

Baker, D.W., Chawla, K.S., and Krizek, R.J. (1993) Compaction fabrics of pelites: experimental consolidation of kaolinite and implications for analysis of strain in slate. *Journal of Structural Geology*, **15**, 1123−1137.

Bernard, S., Horsfield, B., Schulz, H.-M., Schreiber, A., Wirth, R., Vu, T.T.A., Perssen, F., Könitzer, S., Volk, H., Sherwood, N., and Fuentes, D. (2010) Multi-scale detection of organic signatures provides insights into gas shale properties and evolution. *Chemie der Erde*, **70**, 119−133.

Bernard, S., Horsfield, B., Schulz, H.-M., Wirth, R., and Schreiber, A. (2012) Geochemical evolution of organic-rich shales with increasing maturity: a STXM and TEM study of the Posidonia Shale (Lower Toarcian, nothern Germany). *Marine and Petroleum Geology*, **31**, 70−89.

Best, M.E. and Katsube, T. J. (1995) Shale permeability and its significance in hydrocarbon exploration. *The Leading Edge*, **14**, 165−170.

Bilgili, F., Götze, H.-J., Pašteka, R., Schmidt, S., and Hackney,

https://doi.org/10.1346/CCMN.2012.0600308 Published online by Cambridge University Press

R. (2009) Intrusion versus inversion – a 3D density model of the southern rim of the Northwest German Basin. *International Journal of Earth Sciences*, **98**, 571–583.

Bish, D.L. (1993) Rietveld refinement of kaolinite structure at 1.5 K. *Clays and Clay Minerals*, **41**, 738–744.

Curtis, C.D., Lipshie, S.R., Oertel, G., and Pearson, M.J. (1980) Clay orientation in some Upper Carboniferous mudrocks, its relationship to quartz content and some inferences about fissility, porosity and compactional history. *Sedimentology*, **27**, 333–339.

Curtis, M.E., Ambrose, R.J., and Sondergeld, C.H. (2010) Structural characterization of gas shales on the micro- and nano-Scales. *Canadian Unconventional Resources and International Petroleum Conference*, Calgary, Alberta, Canada. ISBN 978-1-55563-217-7.

Day-Stirrat, R., Loucks, R.G., Milliken, K.L., Hillier, S., and van der Pluijm, B. (2008a) Phyllosilicate orientation demonstrates early timing of compactional stabilization in calcite-cemented concretions in the Barnett Shale (Late Mississippian), Fort Worth Basin, Texas (U.S.A). *Clays and Clay Minerals*, **56**, 100–111.

Day-Stirrat, R.J., Aplin, A.C., Środoń, J., and van der Pluijm, B.A. (2008b) Diagenetic reorientation of phyllosilicate minerals in Paleogene mudstones of the Podhale Basin, southern Poland. *Clays and Clay Minerals*, **56**, 100–111.

Deutloff, O., Teichmüller, M., Teichmüller, R., and Wolf, M. (1980) Inkohlungsuntersuchungen im Mesozoikum des Massivs von Vlotho (Niedersächsisches Tektogen). *Neues Jahrbuch für Geologie und Paläontologie Monatshefte*, **6**, 321–341.

Dierick, M., Masschaele, B., and Van Hoorebeke, L. (2004) Octopus, a fast and user-friendly tomographic reconstruction package developed in Lab View®. *Measurement Science and Technology*, **15**, 1366–1370.

Doornenbal, J.C. and Stevenson, A.G. (editors) (2010) *Petroleum Geological Atlas of the southern Permian Basin Area*. European Association of Geoscientists and Engineers Publications BV, Houten, The Netherlands, 354 pp.

Downs, R.T. and Hall-Wallace, M. (2003) The American Mineralogist Crystal Structure Database. *American Mineralogist*, **88**, 247–250.

Draege, A., Jakobsen, M., and Johansen, T.A. (2006) Rock physics modeling of shale diagenesis. *Petroleum Geoscience*, **12**, 49–57.

Elfallagh, F. and Inkson, B.J. (2009) 3D analysis of crack morphologies in silicate glass using FIB tomography. *Journal of the European Ceramic Society*, **29**, 47–52.

Gualtieri, A.F. (2000) Accuracy of XRPD QPA using the combined Rietveld-RIR method. *Journal of Applied Crystallography*, **33**, 267–278.

Heim, S., Guttmann P., Rehbein, S., Werner, S., and Schneider, G. (2009) Energy-tunable full-field X-ray microscopy. Cryo-tomography and full-field spectroscopy with the new BESSY TXM. *Journal of Physics: Conference Series*, **186**, 012041.

Ho, N.-C., Peacor, D.R., and van der Pluijm, B.A. (1995) Reorientation of phyllosilicates in mudstones-to-slate transition at Lehigh Gap, Pennsylvania. *Journal of Structural Geology*, **17**, 345–356.

Ho, N.-C., Peacor, D.R., and van der Pluijm, B.A. (1999) Preferred orientation of phyllosilicates in Gulf Coast mudstones and relation to the smectite-illite transition. *Clays and Clay Minerals*, **47**, 495–504.

Holzner, C., Feser, M., Vogt, S., Hornberger, B., Baines, S.B., and Jacobsen, C. (2010) Zernike phase contrast in scanning microscopy with X-rays. *Nature Physics*, **6**, 883–887.

Hornby, B.E., Schwartz, L.M., and Hudson, J.A. (1994) Anisotropic effective-medium modelling of the elastic properties of shales. *Geophysics* **59**, 1570–1583.

Horsfield, B., Littke, R., Mann, U., Bernard, S., Vu, T., diPrimio, R., and Schulz, H. (2010) Shale Gas in the Posidonia Shale, Hils Area, Germany. *AAPG Search and Discovery Article # 110126*. Adapted from oral presentation at session, Genesis of Shale Gas – Physicochemical and Geochemical Constraints Affecting Methane Adsorption and Desorption, at AAPG Annual Convention, New Orleans, Louisiana, USA, 11–14 April, 2010.

Jenkins, C.D. and Boyer II, C.M. (2008) Coalbed- and Shale-Gas Reservoirs. *Journal of Petroleum Technology*, **60**, 92–99.

Johansen, T.A., Ruud, B.O., and Jakobsen, M. (2004) Effect of grain scale alignment on seismic anisotropy and reflectivity of shales. *Geophysical Prospecting*, **52**, 133–149.

Kanitpanyacharoen, W., Wenk, H.-R., Kets, F., and Lehr, B.C. (2011) Texture and anistropy analysis of Qusaiba shales. *Geophysical Prospecting*, **59**, 536–556.

Keller, L.M., Holzer, L., Wepf, R., and Gasser, P. (2011) 3D Geometry and topology of pore pathways in Opalinus clay: Implications for mass transport. *Applied Clay Science*, **52**, 85–95.

Kus, J., Cramer, B., and Kockel, F. (2005) Effects of a Cretaceous structural inversion and a postulated high heat flow event on petroleum system of the western Lower Saxony Basin and the charge history of the Apeldorn gas field. *Netherlands Journal of Geoscience*, **84**, 3–24.

Leythaeuser, D., Alterbäumer, F.J., and Schaefer, R.G. (1980) Effect of an igneous intrusion on maturation of organic matter in Lower Jurassic shales from NW-Germany. *Physics and Chemistry of the Earth*, **12**, 133–139.

Littke, R. and Rullkötter, J. (1987) Mikroskopische und makroskopische Unterschiede zwischen Profilen unreifen und reifen Posidonienschiefers ans der Hilsmulde. *Facies*, **17**, 171–180.

Littke, R., Baker, D.R., and Leythaeuser, D. (1988) Microscopic and sedimentologic evidence for the generation and migration of hydrocarbons in Toarcian source rocks of different maturities. *Organic Geochemistry*, **13**, 549–559.

Littke, R., Baker, D.R., Leythaeuser, D., and Rullkötter, J. (1991) Keys to the depositional history of the Posidonia Shale (Toarcian) in the Hils Syncline, northern Germany. Pp. 311–333 in: *Modern and Ancient Continental Shelf Anoxia* (R.V. Tyson, editor). Special Publications **58**, Geological Society, London.

Littke, R., Baker, D.R., and Rullkötter, J. (1997) Deposition of petroleum source rocks. Pp. 271–333 in: *Petroleum and Basin Evolution* (D.H. Welte, B. Horsfield, and D.R. Baker, editors). Springer, Heidelberg, Germany.

Lonardelli, I., Wenk, H.-R., and Ren, Y. (2007) Preferred orientation and elastic anisotropy in shales. *Geophysics*, **72**, D33–D40.

Loucks, R.G., Reed, R.M., Ruppel, S., and Jarvie, D.M. (2009) Morphology, genesis, and distribution of nanometer-scale pores in siliceous mudstones of the Mississippian Barnett Shale. *Journal of Sedimentary Research*, **79**, 848–861.

Lutterotti, L., Matthies, S., Wenk, H.-R., Shultz, A.J., and Richardson, J.W. (1997) Combined texture and structure analysis of deformed limestone from time-of-flight neutron diffraction spectra. *Journal of Applied Physics*, **81**, 594–600.

Mann, U. (1987) Veränderung von Mineralmatrix und Porosität eines Erdölmuttergesteins durch einen Intrusivkörper (Lias epsilon 2–3: Hilsmulde, NW-Deutschland). *Facies*, **17**, 181–188.

Mann, U., Leythaeuser, D., and Müller, P.J. (1986) Relation between source rock properties and wireline log parameters: An example from Lower Jurassic Posidonia Shale, NW-Germany. *Organic Geochemistry*, **10**, 1105–1112.

Marone, F., Hintermüller, C., McDonald, S., Abela, R.,

Mikuljan, G., Isenegger, A., and Stampanoni, M. (2009) X-ray Tomographic Microscopy at TOMCAT. *Journal of Physics: Conference Series*, **186**, 012042.

Martini, A.M., Walter, L.M., Ku, T.C.W., Budai, J.M., McIntosh, J.C., and Schoell, M. (2003) Microbial production and modification of gases in sedimentary basins: A geochemical case study from a Devonian shale gas play, Michigan basin. *AAPG Bulletin*, **87**, 1355–1375.

Matthies, S. and Vinel, G.W. (1982) On the reproduction of the orientation distribution function of textured samples from reduced pole figures using the concept of conditional ghost correction. *Physica Status Solidi B*, **122**, K111–K114.

Midgley, P.A., Ward, E.P.W., Hungria, A.B., and Thomas, J.M. (2007) Nanotomography in the chemical, biological and materials sciences. *Chemical Society Reviews*, **36**, 1477–1494.

Militzer, B., Wenk, H.-R., Stackhouse, S., and Stixrude, L. (2011) First-principles calculation of the elastic moduli of sheet silicates and their application to shale anisotropy. *American Mineralogist*, **96**, 125–137.

Muñoz, Y.A., Littke, R., and Brix, M.R. (2007) Fluid systems and basin evolution of the western Lower Saxony Basin, Germany. *Geofluids*, **7**, 335–355.

Plançon, A., Tsipurski, S.I., and Drits, V.A. (1985) Calculation of intensity distribution in the case of oblique texture electron diffusion. *Journal of Applied Crystallography* **18**, 191–196.

Petmecky, S., Meier, L., Reiser, H., and Littke, R. (1999) High thermal maturity in the Lower Saxony Basin: Intrusion or deep burial? *Tectonophysics*, **304**, 317–344.

Rietveld, H.M. (1969) A profile refinement method for nuclear and magnetic structures. *Journal of Applied Crystallography*, **2**, 65–71.

Rullkötter, J., Leythaeuser, D., Horsfield, B., Littke, R., Mann, U., Müller, P.J., Radke, M., Schaefer, R.G., Schenk, H.-J., Schwochau, K., Witte, E.G., and Welte, D.H. (1988) Organic matter maturation under the influence of a deep intrusive heat source: A natural experiment for quantitation of hydrocarbon generation and expulsion from a petroleum source rock (Toarcian shale, northern Germany). *Organic Geochemistry*, **13**, 847–856.

Sayers, C.M. (1994) The elastic anisotropy of shales. *Journal of Geophysical Research*, **99**, 767–774.

Schulz, H.-M., Horsfield, B., and Sachsenhofer, R.F. (2010) Shale gas in Europe: a regional overview and current research activities. *Petroleum Geology Conference series*, **7**, 1079–1085.

Sintubin, M. (1994) Clay fabrics in relation to the burial history of shales. *Sedimentology*, **41**, 1161–1169.

Slaughter, M. and Hill, R.J. (1991) The influence of organic matter in organogenic dolomization. *Journal of Sedimentary Research*, **61**, 296–303.

Stampanoni, M., Groso, A. Isenegger, A., Mikuljan, G., Chen, Q., Bertrand, A., Henein, S., Betemps, R., Frommherz, U., Böhler, P., Meister, D., Lange, M., and Abela, R. (2006) Trends in synchrotron-based tomographic imaging: the SLS experience. In: Developments in X-ray Tomography V Ulrich Bonse (editor). *Proceedings of SPIE*, **6318**, 63180M.

Tissot, B.O. and Welte, D.D. (1984) *Petroleum Formation and Occurrence*, 2nd edition. Springer-Verlag, Berlin.

Valcke, S.L.A., Casey, M., Lloyd, G.E., Kendall, J.-M., and Fisher, Q.J. (2006) Lattice preferred orientation and seismic anisotropy in sedimentary rocks. *Geophysical Journal International*, **166**, 652–666.

Vernik, L. (1993) Microcrack-induced versus intrinsic elastic anisotropy in mature hc-source shales. *Geophysics*, **58**, 1703–1706.

Vernik, L. (1994) Hydrocarbon-generation-induced microcracking of source rocks. *Geophysics*, **59**, 555–563.

Vernik, L. and Nur, A. (1992) Ultrasonic velocity and anisotropy of hydrocarbon source rock. *Geophysics*, **57**, 727–735.

Voltolini, M., Wenk, H.-R., Mondol, N.H., Bjørlykke, K., and Jahren, J. (2009) Anisotropy of experimentally compressed kaolinite-illite-quartz mixtures. *Geophysics*, **74**, 13–23.

Wang, Y., De Carlo, F.D., Mancini, C., McNulty, I., Tieman, B., Bresnahan, J., Foster, I., Insley, J., Lane, P., von Laszewski, G., Kesselman, C., Su, M.-H., & Thiebaux, M. (2001) A high-throughput X-ray microtomography system at the Advanced Photon Source. *Review of Scientific Instruments*, **72**, 2062–2068.

Wenk, H.-R., Matthies, S., Donovan, J., and Chateigner, D. (1998) Beartex: A windows-based program system for quantitative texture analysis. *Journal of Applied Crystallography*, **31**, 262–269.

Wenk, H.-R., Voltolini, M., Mazurek, M., Loon, L.R.V., and Vinsot, A. (2008) Preferred orientations and anisotropy in shales: Callovo-Oxfordian shale (France) and Opalinus clay (Switzerland). *Clays and Clay Minerals*, **56**, 285–306.

Wenk, H.-R., Kanitpanpanyacharoen, W., and Voltolini, M. (2010) Preferred orientation of phyllosilicates: Comparison of fault gouge, shale and schist. *Journal of Structural Geology*, **32**, 478–489.

(*Received 18 July 2011; revised 1 May 2012; Ms. 590; AE: W. Huff*)